Materials and Solidification

Research Article

Magnetic heat-treatment induced uniaxial magnetic anisotropy and dynamic precipitation in Fe–Ga magnetostrictive alloys

Ying Chen[1], Ruihua Qiao[1], Junming Gou[1], Tie Liu[2], Qiang Wang[2], Tianyu Ma[1,✉]

Cite this article: Chen Y, Qiao R, Gou J, et al. *Materials and Solidification* 2025, **1**(1): 9580004. https://doi.org/10.26599/MAS.2025.9580004

ABSTRACT: Introducing coherent tetragonal nanoprecipitates into a cubic matrix has recently been found to significantly increase the magnetostriction of Fe-based alloys. Combining this novel strategy with conventional approaches, such as the introduction of uniaxial magnetic anisotropy (uniaxial alignment of magnetic domains), may improve the magnetostriction performance. On the basis of this consideration, a large-magnetostriction alloy, $Fe_{73}Ga_{27}$ (at%), was subjected to magnetic heat treatment (MHT) to introduce uniaxial anisotropy and nanoprecipitates simultaneously. The results showed that strong uniaxial magnetic anisotropy (well-aligned magnetic domains) is induced together with the formation of dense nanoprecipitates, hence improving the magnetostriction from 65 ppm for the solution-treated (ST) counterpart to 140 ppm by 115%. However, such magnetostriction enhancement effect is weaker than that observed in the sample subjected to heat treatment for the same time at the same temperature in the absence of a magnetic field. Further microstructural investigations revealed that compared with isothermal annealing, MHT led to dynamic precipitation, the formation of coarser and incoherent tetragonal nanoprecipitates and even a face-centered cubic (FCC) equilibrium phase with intrinsic negative magnetostriction. These results suggest that the magnetic field provides an extra driving force to accelerate precipitation kinetics and that the magnetic annealing conditions should be carefully controlled to prevent the overgrowth of tetragonal nanoprecipitates to enhance the magnetostriction performance.

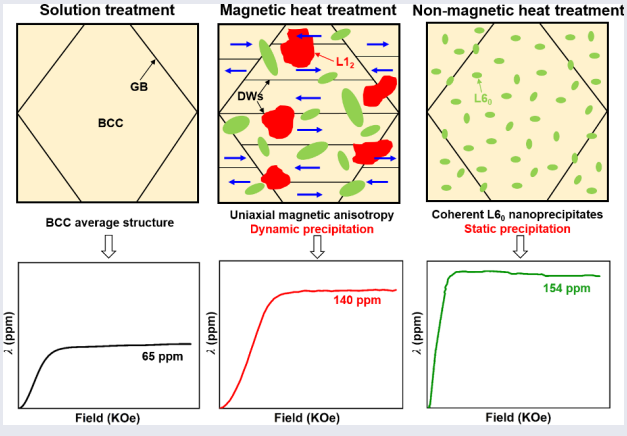

KEYWORDS: magnetostrictive materials; precipitation; magnetic heat treatment (MHT); microstructure

1 Introduction

Materials with large magnetostriction (large magnetic field-induced strain) can expand or contract under an external magnetic field, thus making them useful for actuators, sensors and energy-harvesting devices [1–3]. Recently, beyond the prototype magnetostrictive materials based on brittle rare-earth transient-metal intermetallic compounds (a well-known example is $Tb_{0.3}Dy_{0.7}Fe_2$ alloy, commerially known as Terfenol-D [4]), a special class of materials based on Fe-alloys (such as Fe–Ga [5], Fe–Mo [6], and Fe–Al [7]) has attracted much attention owing to their better ductility and smaller switching field. The large magnetostriction of these materials is also sensitive to nanoscale structural heterogeneities [8,9] in addition to spin–orbit coupling (the origin of homogeneous magnetostrictive materials, such as Terfenol-D [10]). For example, in the extensively studied system Fe–Ga, introducing coherent $L6_0$-type tetragonal nanoprecipitates into the body-centered cubic (BCC) matrix either by alloying rare-earth elements [11] or by short-term isothermal aging [12] can significantly increase magnetostriction by more than three-fold. The nanodispersive precipitates can not only distort the mechanically subsequent BCC matrix via coherent elastic interactions, substantially enhancing saturation magnetostriction [13,14], but also reduce the net magnetocrystalline anisotropy (MCA) via random magnetic interactions, effectively reducing the switching field [15], thus enabling large and sensitive magnetostriction performance that is highly desirable for applications. Consequently, there is great interest in achieving high-performance magnetostriction by engineering nanoprecipitates in this special class.

There are also conventional approaches to enhance magnetostriction, called "grain orientation" and "domain orientation" engineering [16]. "Grain orientation" engineering refers to the growth of oriented crystals with all grains along or

[1] Frontier Institute of Science and Technology, State Key Laboratory for Mechanical Behavior of Materials, Xi'an Jiaotong University, Xi'an 710049, China. [2] Key Laboratory of Electromagnetic Processing of Materials (Ministry of Education), Northeastern University, Shenyang 110819, China.

✉ Corresponding author. E-mail: matianyu@xjtu.edu.cn

Received: October 10, 2024; Revised: December 7, 2024; Accepted: January 17, 2025

close to the easy magnetization direction (EMD), along which the magnetostriction constant is the largest [17–20]. The "domain orientation" engineering refers to the constrained domain configuration with magnetic domains aligned along one specific direction (the so-called uniaxial magnetic anisotropy) so that the subsequent magnetization process involves only 90° domain switches, avoiding 180° domain switches for a thermally demagnetized state (in which the magnetic domains are aligned along equivalent EMDs on average) that cannot contribute to magnetostriction [21,22]. In general, the constrained domain configuration can be realized by cooling the magnetostrictive material in an external magnetic field across its Curie temperature (T_C). The physical principle is that the MCA is relatively weak in the vicinity of T_C. Thus, the domains can be easily aligned along the external magnetic field direction [23]. For example, the magnetostriction of Terfenol-D polycrystals can be enhanced after magnetic annealing [24,25]. Therefore, there is a simple motivation: If coherent tetragonal nanoprecipitates were introduced into a cubic matrix with an aligned magnetic domain state, one could achieve better magnetostriction performance in heterogeneous Fe-based magnetostriction alloys, such as Fe–Ga. This approach is technically feasible because the nanoprecipitates can be formed, and magnetic domains can be realigned simultaneously by performing magnetic tempering at temperatures above the effective nucleation temperature (T_{nd}) of the precipitates and by performing magnetic cooling across T_C of the matrix.

On the basis of this consideration, here, we attempt to introduce both tetragonal nanoprecipitates and uniaxial magnetic anisotropy simultaneously by selecting a proof-of-principle reference, $Fe_{73}Ga_{27}$ (at%) alloy. This alloy was selected for the following reasons. First, the solution-treated (ST) $Fe_{73}Ga_{27}$ alloy is known to exhibit peak magnetostriction in the Fe–Ga system and has faster $L6_0$ precipitation kinetics than the other peak-magnetostriction composition $Fe_{81}Ga_{19}$ [9]. Second, previous work [26] has shown that the nose temperature (T_n) for the precipitation of $L6_0$ nanoprecipitates is ~400 °C, which is slightly higher than T_C of the cubic matrix (as shown in Fig. 1(a)), thus making it possible to simultaneously introduce $L6_0$ nanoprecipitates and uniaxial magnetic anisotropy by performing magnetic tempering and cooling at temperatures above 400 °C. More importantly, although magnetic heat treatment (MHT) was found to enhance the magnetostriction of Fe–Ga alloys [27], the reason has been attributed merely to magnetic domain realignment (induced magnetic anisotropy), and the precipitation of $L6_0$ phase that could concurrently occur has not been discussed in the past. Herein, we performed a comparative study on bulk $Fe_{73}Ga_{27}$ polycrystals by holding the sample at the same temperature for the same time and then cooling to room temperature at the same rate in the presence and absence of an external magnetic field, 12 T. The differences in microstructure (especially the morphology and structure of precipitates) and magnetic domain configuration between them were investigated, and their differential influences on magnetostriction performance were also discussed.

2 Experimental

Ingots with a nominal composition of $Fe_{73}Ga_{27}$ were prepared via the induction melting of Fe and Ga metals with a purity of 99.99% in an argon atmosphere and then cast into a copper mold with an inner diameter of 12 mm. After two ends were cut with a casting shrinkage cavity and surface contamination was removed, the rod with a length of 120 mm was then sealed in quartz tubes filled with high-purity argon and subsequently homogenized for 72 h at 1100 °C, followed by quenching in ice-water. According to previous work [28,29], ST state of this alloy bears a BCC average structure, consisting mainly of $D0_3$ phase and a minority of A2 phase. Using a vibrating sample magnetometer (Lakeshore7407, Lake Shore Cryotronics, USA), the magnetization vs. temperature (M–T) curve of ST sample was measured (Fig. 1(a)) upon heating at 5 °C/min under 2 kO, from which the T_C of $D0_3$ phase, the subsequent A2/$D0_3$ to $L1_2$ phase transition temperature, and $L1_2$ to $D0_{19}$ phase transition temperature [29] were determined and are shown in Fig. 1(a). The samples were further heat-treated on the basis of these temperatures. Two sections with the diamter of 12 mm and length of 40 mm cut from the same ST rod were subjected to further heat treatments. The same furnace (JMTD-6-30, Jastec, Japan), around which a strong magnetic field of 12 T can be provided, was used to conduct heat treatments. As illustrated in Fig. 1(b), each sample was heated to 450 °C (above T_C-$D0_3$ and within the temperature scope of A2/$D0_3$ to $L1_2$ phase transition), held for 1 h, and then cooled to room temperature. The selection of 1 h annealing time was based on our previous work [6,12], since annealing at this temperature for 1 h resulted in a magnetostriction peak for random polycrystalline $Fe_{73}Ga_{27}$. The difference is that one sample was heat-treated in the presence of 12 T at 450 °C and cooled through T_C-$D0_3$ (red segment shown in

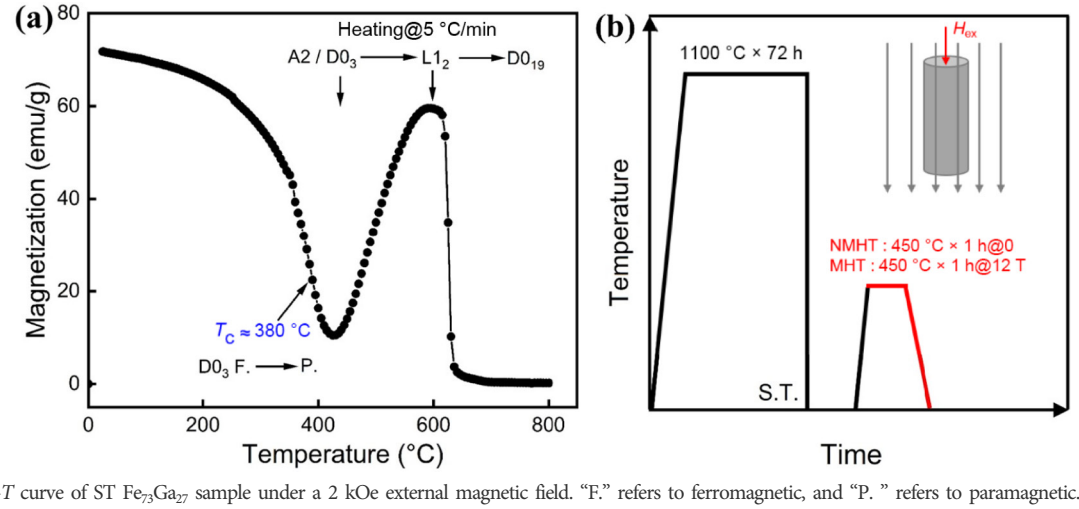

Fig. 1 (a) M–T curve of ST $Fe_{73}Ga_{27}$ sample under a 2 kOe external magnetic field. "F." refers to ferromagnetic, and "P. " refers to paramagnetic. (b) Schematic illustration of heat-treatment procedure. Inset is a schematic illustration of MHT under 12 T and NMHT under 0 T.

Fig. 1(b)), and the other was heat-treated in the absence of a magnetic field. The treatment magnetic field (H_{ex}) was applied along the rod length direction, which was expected to produce the precipitation of $L6_0$ (intermediate phase of $L1_2$) and realign the magnetic domains of BCC matrix simultaneously. To distinguish these two conditions, one is referred to as MHT, and the other is referred to as nonmagnetic heat treatment (NMHT).

Optical micrograph observations revealed that the present MHT does not influence the grain size or texture of the present random polycrystalline sample. Therefore, the possible influence of grain size/texture on magnetostriction was not considered in this work. The average structure of the samples was identified via an X-ray diffractometer (XRD; 7000, Shimadzu, Janpan) with Cu Kα radiation. The 2θ angle range was from 30° to 90°, which was facilitated at a controlled scanning rate of 2 (°)/min. Using a physical property measurement system (PPMS; 14LH-9T, Quantum Design, USA) magnetometer, magnetization curves were measured by setting the measurement field direction (H_m) along and perpendicular to H_{ex} to characterize the possible uniaxial magnetic anisotropy. A sample with a size of 10 mm × 2 mm × 1 mm was cut from the heat-treated sample. The parallel magnetostriction of the sample was measured via the standard strain gauge technique. To avoid surface damage induced by mechanical grinding, the sample surface was carefully polished with water-based diamond suspensions, followed by a vibration polisher (Buehler, Vibromet 2, USA) with 0.1 μm colloidal silica polishing suspensions. Transmission electron microscopy (TEM) foil samples were prepared via a twin-jet electropolisher (MTP-1A, Jiaoda, China) at temperatures below 243 K, followed by ion milling to remove surface contamination. The microstructure and magnetic domain configuration were characterized via TEM (JEM-2100F, JEOL, Japan) at 200 kV. Digital micrograph software (version 3.21.1374.0, Gatan, Inc., USA) was used to analyze the high-resolution TEM (HR-TEM) images. The magnetic domain structure was observed via the Fresnel method.

3 Results

Figure 2(a) shows the magnetostriction curves of $Fe_{73}Ga_{27}$ samples in ST state and with MHT. The saturation parallel magnetostriction $\lambda_{//s}$ (technical strain along the measurement direction) is 65 ppm in ST state and significantly increases to 140 ppm after MHT, and the corresponding increase ratio is ~115%. This demonstrates that MHT is also effective in enhancing the magnetostriction of Fe–Ga polycrystalline samples, similar to that observed in oriented single crystals [30]. However, the magnetostriction enhancement effect induced by MHT is weaker than that induced by NMHT for the same time at the same temperature. As shown by the green curve in Fig. 2(a), $\lambda_{//s}$ of the NMHT sample is 154 ppm, which is ~137% greater than that of ST sample. In addition, the saturation magnetic field of the magnetostriction curve of the MHT sample is greater than that of the NMHT sample. In homogeneous ferromagnets, MHT can induce uniaxial magnetic anisotropy, which not only enhances magnetostriction but also strengthens effective magnetocrystalline anisotropy. Since the saturation field is proportional to the effective MCA, MHT usually contributes to increasing the saturation magnetic field [31,32]. Note that Fe-Ga is a heterogeneous ferromagnet, and its microstructure can be tailored by heat treatment [9]. In the following, we show that MHT of heterogeneous Fe–Ga alloys not only induces uniaxial magnetic anisotropy but also changes structural heterogeneities, which helps in understanding the differences in magnetostriction and saturation fields between MHT and NMHT samples.

The uniaxial magnetic anisotropy can be characterized by the measurement-direction dependence of the magnetization and by the constrained magnetic domain configuration. Figure 2(b) shows the M–H hysteresis loops of $Fe_{73}Ga_{27}$ samples in ST state and with MHT. The red and blue curves represent those of MHT sample with H_m parallel and perpendicular to H_{ex}, respectively. Since Fe–Ga is a soft ferromagnet, the present field of 20 kOe is sufficient to magnetize the MHT sample to a saturated state along either the parallel or perpendicular direction. Note that the magnetization curves of these two cases do not overlap with each other before reaching the saturation state, demonstrating the existence of uniaxial magnetic anisotropy induced by MHT [33,34]. Owing to the uniaxial magnetic anisotropy, applying a parallel field excludes the 90° domain rotation process, whereas applying a perpendicular field still evolves 90° domain rotation process. As a result, it will be easier to approach the saturation state (exhibiting a larger slope in the M–H curve at low-field regions) for measuring parallel to the MHT field direction than for measuring perpendicularly. This measurement direction dependence of the magnetization process is unlike that for the thermally demagnetized random-polycrystalline sample, where the magnetization curves are measured along two directions with a 90° overlap with each other. In addition, the saturation magnetization (M_s) is ~135 emu/g for the MHT sample, which is 11% higher than that of the ST sample (~122 emu/g). This indicates that a new phase with higher magnetization than the BCC matrix also formed after MHT. As reported in Refs. [12,29,35], this increase can be attributed to the formation of $L6_0/L1_2$ phases toward equilibrium.

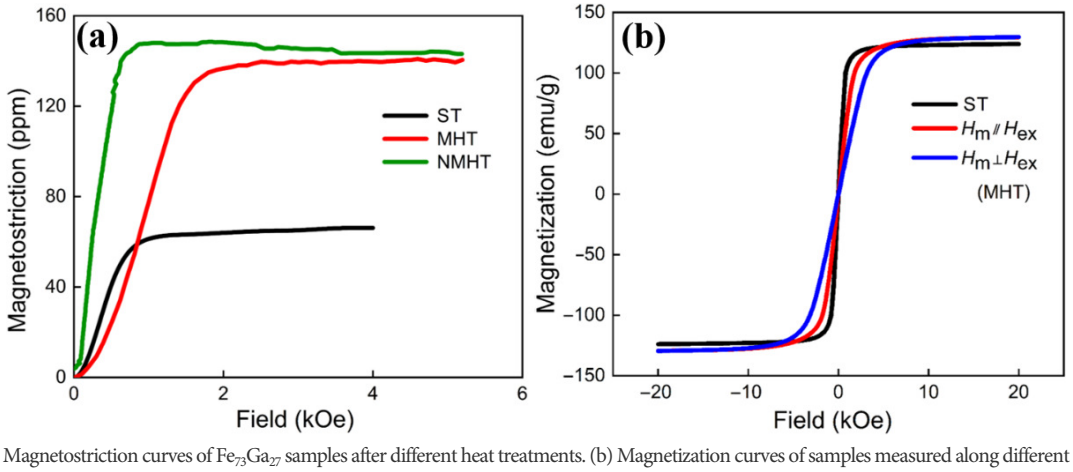

Fig. 2 (a) Magnetostriction curves of $Fe_{73}Ga_{27}$ samples after different heat treatments. (b) Magnetization curves of samples measured along different directions.

Figures 3(a) and 3(b) show de- and over-focus Lorentz-TEM (L-TEM) Fresnel images of the MHT sample, where the white or black contrasts opposite those displayed in the de- and over-focus images are magnetic domain walls (DWs). The magnetic DWs exhibit straight lines in this sample. The magnetic DWs are nearly parallel to each other, indicating that they are 180° DWs. Therefore, the magnetization vectors of adjacent domains separated by these 180° DWs are opposite to each other. This means that the domains are constrained along the treating field direction, further confirming the uniaxial magnetic anisotropy induced by MHT. This configuration is unlike that at the thermally demagnetized state, for which the magnetic domains are averagely distributed along EMDs, i.e., the six equivalent <100> axes for Fe–Ga alloys [36].

For comparison, we investigated the magnetic domain configurations for the NMHT sample in the thermally demagnetized state, as shown in Figs. 3(c) and 3(d). It has a disordered magnetic domain configuration, where the magnetizations between adjacent domains are not antiparallel to each other, unlike the well-aligned, ordered domain configuration of the MHT sample. In addition, DWs are not straight lines but are twisted. As discussed in our previous work [12], such twisted magnetic DWs are formed due to random exchange coupling (short-range magnetic interactions) between the dispersive nanoprecipitates formed during the NMHT process and the BCC matrix, which results in the collapse of the net MCA and contributes to more sensitive magnetostriction. Note that, compared with those of the MHT sample, the sizes of the nanoprecipitates are smaller for the NMHT sample, and most nanoprecipitates are coherent with the matrix. This comparison indicates that the 12 T external magnetic field applied during the heat treatment process not only induces strong uniaxial magnetic anisotropy but also induces dynamic precipitation of the secondary phase.

Prior to presenting the microstructure difference between the MHT and NMHT samples, the precipitation of the $L6_0/L1_2$ phases in the Fe–Ga alloys occurred via a diffusive-displacive mixed-mode phase transformation mechanism [35]. The complete transformation from BCC ($A2/D0_3$) metastable phase to the $L1_2$ equilibrium phase requires both atomic diffusion ($\varepsilon_a \approx -11\%$) and drastic Bain distortion ($\varepsilon_c \approx 26\%$) [37,38] and has extremely slow kinetics [39–41]. $L6_0$ nanoprecipitates have been suggested as precursors of the ordered face-centered cubic (FCC) $L1_2$ equilibrium phase [12,42], which refers to a state in which the atomic diffusion may have already finished but the lattice parameters are constrained at the early transformation stage. Experimental studies revealed that the $L6_0$ nanoprecipitates exhibit size-dependent tetragonality ranging from $1/\sqrt{2}$ (for ideal BCCs) to 1 (for ideal FCC) [42], characterized by a gradual increase in {111}-$L6_0$ lattice spacing during their growth and further transformation toward equilibrium $L1_2$.

Figure 4 shows the XRD patterns of the samples subjected to different heat treatments. ST sample has a BCC average structure, as judged from the corresponding {110}, {200}, and {211} fundamental reflections at 2θ angles of ~43.5°, ~63.2°, and ~80.2°, respectively. The lattice parameter a is 0.29 nm if these reflections are indexed as the A2 phase. According to previous electron diffraction studies [29,43], the ordered-BCC $D0_3$ phase evolved within the ST sample, and these fundamental reflections can also be indexed as {220}, {400}, and {422} for the $D0_3$ phase. For the NMHT and MHT samples, extra weak reflections are observed at Bragg angles smaller than those for {110}-BCC, which can be indexed as the {111} reflection of the $L6_0/L1_2$ phases [44]. Comparably, the intensity of this extra peak is weaker for the NMHT sample than for the MHT sample, indicating that the presence of a 12 T magnetic field during the heat treatment process promotes the precipitation of the $L6_0/L1_2$ phases, i.e., increases their volume fraction. In addition, the 2θ angle of {111} reflection is ~43.2° for the NMHT sample, which is larger than the ~42.2° for the MHT sample. The lattice spacing d-{111} ≈ 0.209 nm ($L6_0$) for the NMHT sample is smaller than the d-{111} ≈ 0.214 nm ($L1_2$) for the MHT sample. Therefore, the weak reflection in the NMHT is attributed to the nonequilibrium $L6_0$ phase, not the equilibrium $L1_2$ phase. Note that the $L6_0$ nanoprecipitates have size-dependent tetragonality [42]. The larger its size is, the greater its tetragonality. The small $L6_0$ nanoprecipitates may not be distinguished by XRD since their reflections could overlap with those of the BCC matrix. This finding also indicates that the presence of a 12 T magnetic field during the heat treatment process makes it easier for the precipitate structure to reach equilibrium at $L1_2$. This result is consistent with the morphology shown in Fig. 3, in which the MHT sample contains larger nanoprecipitates than the NMHT sample does.

We performed further TEM characterization to identify the

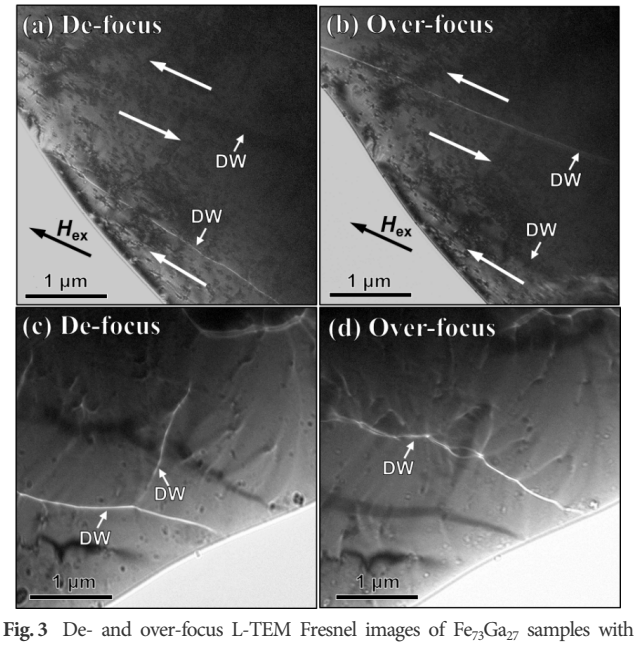

Fig. 3 De- and over-focus L-TEM Fresnel images of $Fe_{73}Ga_{27}$ samples with (a, b) MHT and (c, d) NMHT.

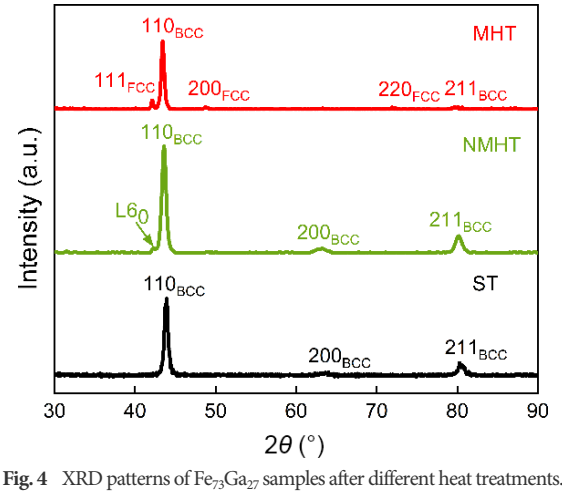

Fig. 4 XRD patterns of $Fe_{73}Ga_{27}$ samples after different heat treatments.

nanoprecipitates, focusing on the differences in size and structure between the NMHT and MHT samples. Figure 5 shows the TEM results for the NMHT sample. In the bright-field image taken along the {111}-BCC zone axis (Fig. 5(a)), dispersive $L6_0$ nanoprecipitates are embedded within the matrix. This is due to the size-dependent tetragonality of the $L6_0$ nanoprecipitates, where the smaller nanoprecipitates have tetragonality slightly greater than $1/\sqrt{2}$ (for ideal BCCs) and the larger nanoprecipitates have tetragonality close to 1 (for equilibrium $L1_2$). In the corresponding selected area electron diffraction (SAED) pattern (Fig. 5(b)), weak diffraction spots can be observed at the 1/2 position due to the formation of a small fraction of $L6_0$ nanoprecipitates. According to the Bain orientation relationship, $[\bar{1}11]$-$D0_3$//$[\bar{1}01]$-$L6_0$ and $(\bar{2}20)$-$D0_3$//(020)-$L6_0$, these weak diffraction spots can be indexed as {010} and {101} superlattice reflections for three-equivalent $L6_0$ variants. Since most nanoprecipitates are coherent with the BCC matrix, the fundamental reflections of $L6_0$ variants overlap with the {220}-BCC reflections.

Figure 6 shows the TEM results for the MHT sample. In the bright-field image (Fig. 6), the sample still has a heterogeneous microstructure, and the precipitates in the dark or bright contrasts are much coarser than those observed in the NMHT sample. In addition, the nanoprecipitates vary greatly in size. For example, the sizes of finer precipitates within the white circle region are less than 100 nm, whereas the sizes of coarser precipitates within the blue circle region are greater than 1 μm. The corresponding SAED pattern (Fig. 6(b)) reveals that the white region contains a BCC matrix and coherent $L6_0$ nanoprecipitates, as judged by the 1/2 weak diffraction spots indicated by red arrows. The SAED pattern (Fig. 6(c)) of the coarse precipitate region (blue region in Fig. 6(a)) reveals the coexistence of $L1_2$ twins and the BCC matrix. As indexed in Fig. 6(a), the strong spots are attributed to the twin set of $L1_2$ variants sharing {111} as their twin plane, and the extra weak spots indexed in white are attributed to the untransformed BCC matrix surrounding the $L1_2$ twin variants. Since the bright-field image in Fig. 6(a) was taken by tilting the beam incidence along the {110} direction of the $L1_2$ twin variants (inside the blue circle), the $L1_2$ twin variants are in dark contrast, which can then be distinguished from the surrounding BCC matrix and other $L1_2$ variants in brighter contrasts. Figure 6(d) shows a higher magnification bright-field image taken along the same beam incidence, which reveals a larger number of $L1_2$ twin variants, which are named V1 and V2. As reported in our previous work [42], $L6_0$ nanoprecipitates have size-dependent tetragonality. The larger its size is, the greater its tetragonality, i.e., its tetragonality c/a varies from $1/\sqrt{2}$ (0.707) for the ideal BCC to 1 for the equilibrium phase $L1_2$. Thus, the fine nanoprecipitates formed at the early stage have small tetragonality, which is coherent with the BCC matrix, whereas the coarse nanoprecipitates at the later stage have greater tetragonality, which is incoherent with the BCC matrix. Figures 6(e) and 6(f) show dark-field images of $L1_2$ variants, where sharp {111} twin boundary separates V1 and V2. In addition, the dark field images also reveal heterogeneous morphology and SFs inside $L1_2$ variants, which are typical features led by mixed-mode phase transformation, as reported in our previous work [36].

The above characterizations clearly reveal that MHT can simultaneously induce uniaxial magnetic anisotropy and dynamic precipitation, thus enabling greater magnetostriction than the parent state of ST. However, its magnetostriction is lower than that of the NMHT sample. We have yet to find that they exhibit obvious differences in both domain configuration and microstructure. In the next section, we explain in detail why applying a strong magnetic field during the heat treatment process cannot result in a magnetostriction-strengthening effect comparable to that of NMHT processing.

4 Discussion

In a homogeneous cubic ferromagnet with {100} EMD (BCC-structured Fe is one example of this type), tetragonal lattice distortion occurs during the Curie transition, i.e., spontaneous magnetization process [45], generating a lattice strain $\varepsilon = (c-a)/a$ along the [001] axis, where c and a are the long and short axes of the tetragonal lattice, respectively. $\varepsilon = (c-a)/a$ is also called the spontaneous magnetostriction constant λ_{001}. In homogeneous ferromagnets with cubic structures, the magnetostriction generated by tetragonal lattice distortion during the Curie transition can be expressed by Eq. (1) [46–48]:

$$\lambda_{//s} = \frac{3}{2}\lambda_{[001]}\begin{bmatrix} n_y+n_z & -n_y & -n_z \\ -n_x & n_x+n_z & -n_z \\ -n_x & -n_y & n_x+n_y \end{bmatrix} \quad (1)$$

where $\lambda_{[001]}$ is the magnetostriction constant measured along the [001] direction for a single crystal; n_x, n_y, and n_z are the volume fractions of the domains along $[100]/[\bar{1}00]$, $[010]/[0\bar{1}0]$, or $[001]/[00\bar{1}]$ directions with the constraint $n_x + n_y + n_z = 1$. The

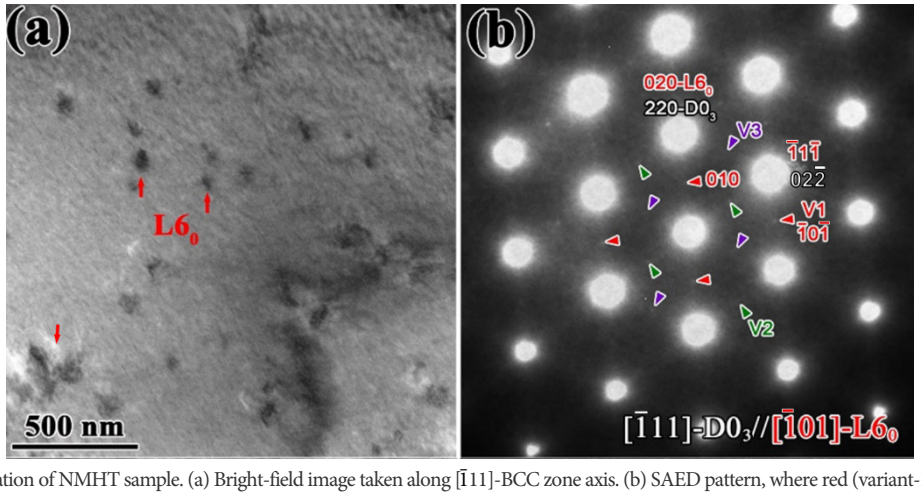

Fig. 5 TEM characterization of NMHT sample. (a) Bright-field image taken along $[\bar{1}11]$-BCC zone axis. (b) SAED pattern, where red (variant-1), green (variant-2), and purple (variant-3) arrows indicate superlattice reflections of $L6_0$ variants.

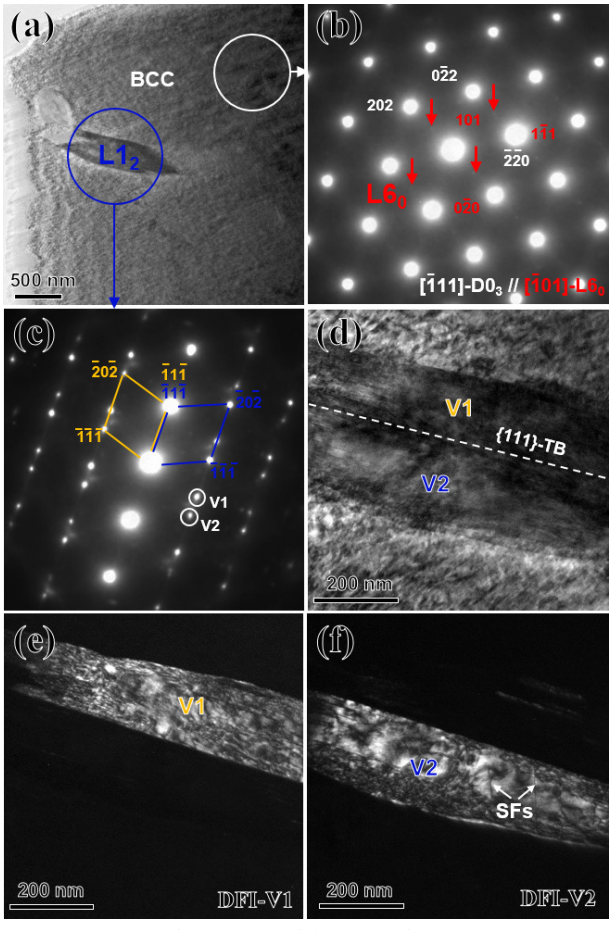

Fig. 6 (a) Low-magnification bright-field image of MHT sample. (b) SAED pattern of white circle region in (a), taken by tilting BCC matrix along [$\bar{1}$11] zone axis. Red arrows indicate superlattice reflections for coherent $L6_0$ nanoprecipitates. (c) SAED pattern of blue circle region in (a), taken by tilting $L1_2$ variants along {110} zone axis. (d) High-magnification bright-field image and (e, f) dark-field images of region containing $L1_2$ twin variants, taken from reflections indicated by white circles in (c), respectively. "SFs" refer to stacking faults.

rows correspond to the [100], [010], and [001] field directions (or their opposite directions), and the columns correspond to the [100], [010], and [001] measurement directions for magnetostriction. In the thermally demagnetized state, the magnetic domains inside a single crystal are aligned along six equivalent EMDs (i.e., [001], [100], [010], [00$\bar{1}$], [$\bar{1}$00], and [0$\bar{1}$0]), as shown in the upper channel of Fig. 7(a) (where the domains perpendicular to the view direction are not shown), with $n_x = n_y = n_z = 1/3$. When an external field is applied along the horizontal direction (e.g., [001]), both 90° and 180° domain switches occur via DW (domain wall) motion and domain rotation, forming a single domain state, such as that shown in the bottom channel of Fig. 7(a). The saturation technical strain $\lambda_{//s}$ equals $\lambda_{[001]}$, according to Eq. (1). Since the motion of 180° DWs does not contribute to magnetostriction, the magnetostriction generated by the 90° domain switches from 4 of the 6 kinds of domains ([100], [010], [$\bar{1}$00], and [0$\bar{1}$0] domains) $\lambda_{//s}$ is then 2/3 $(c/a - 1)$ [47,48]. When an external magnetic field is applied during cooling through T_C, the magnetic domains are constrained along a specific direction, i.e., forming uniaxial magnetic anisotropy, such as that shown in the upper channel of Fig. 7(b). Supposing that the MHT field direction was along [100], there would be only [100] and [$\bar{1}$00] domains, which means that $n_x = 1$, $n_y = n_z = 0$. Upon the subsequent magnetization process by applying a magnetic field along the horizontal direction (e.g., [001] direction), only a 90° domain switch occurs, and $\lambda_{//s}$ is 3/2 $\lambda_{[001]}$ [9,21,49], similar to that shown in the bottom channel of Fig. 7(b). This is also the theoretical magnetostriction limit that a homogeneous ferromagnet can reach. Theoretically, the saturation strain of induced uniaxial anisotropy can be increased to 1.5 times that in the thermally demagnetized state.

For heterogeneous ferromagnets, introducing coherent tetragonal nanoprecipitates can distort the soft cubic matrix locally due to the mutual elastic interaction between them [50]. This phenomenon increases the average tetragonality of the matrix lattice, i.e., the spontaneous magnetostriction constant λ_{001}. Fe–Ga alloys are one example of this type, in which nanosized L60-type tetragonal nanoprecipitates have been identified by various techniques [11,13,29,51]. When the $L6_0$ nanoprecipitates are smaller than the effective exchange interaction length between $L6_0$ and the BCC matrix, the magnetizations of both the $L6_0$ nanoprecipitates and the BCC matrix can slip in an external magnetic field [52], as shown in Fig. 7(c). Owing to the increased spontaneous magnetostriction constant (described here in terms of λ'_{001}, which depends on the size, tetragonality, and coherency of the nanoprecipitates), the obtained $\lambda_{//s}$ (2/3 λ'_{001}, for a single crystal) is larger than that for the nanoprecipitate-free matrix (i.e., 2/3 λ_{001}). As reported in our recent work [26], by optimizing the size, tetragonality, and coherency of $L6_0$ nanoprecipitates in Fe–Ga alloys, the magnetostriction enhancement ratio can be doubled (~200%). In addition, the fine $L6_0$ precipitates can also randomly coupled with the matrix via short-range magnetic interactions, resulting in the collapse of the net MCA [52]. Therefore, the NMHT sample has a lower saturation magnetic field than its ST counterpart.

Therefore, inducing both uniaxial magnetic anisotropy and coherent nanoprecipitates can enhance magnetostriction. However, the magnetostriction enhancement ratios for both the NMHT and MHT samples (when compared with their ST counterparts) are smaller than the theoretical values mentioned above. For the NMHT sample with nanoprecipitates only, the obtained magnetostriction $\lambda_{//s}$ of 154 ppm is smaller than the optimum magnetostriction of 180 ppm in the same $Fe_{73}Ga_{27}$ alloy after isothermal aging for 1 h at 400 °C and subsequent quenching [26]. This can be attributed to the formation of some incoherent $L6_0$ nanoprecipitates (Figs. 3(c), 3(d), and 5(a)) because isothermal aging at a temperature (450 °C for the present work) higher than its T_n (~400 °C) accelerated the growth of $L6_0$ nanoprecipitates. When the size of $L6_0$ nanoprecipitates is greater than a critical value, the enlarged tetragonality makes them incoherent with the BCC matrix. As a result, the weakened elastic interaction between the incoherent nanoprecipitates and the BCC matrix deteriorates the spontaneous magnetostriction constant λ'_{001} of the matrix. For the MHT sample with both uniaxial magnetic anisotropy and nanoprecipitates, the magnetization process is schematically illustrated in Fig. 7(d), from which the obtained $\lambda_{//s}$ should be 3/2 λ''_{001}. However, compared with that of ST counterpart, its magnetostriction enhancement is just 115%, which is smaller than that either for inducing uniaxial magnetic anisotropy or for inducing coherent tetragonal nanoprecipitates. This can be attributed to two reasons: i) the spontaneous magnetostriction constant λ''_{001} resulting from the introduction of coarse $L6_0$ nanoprecipitates (Figs. 3(a) and 3(b)) is much smaller than λ'_{001} resulting from the introduction of fine and coherent $L6_0$ nanoprecipitates, and ii) the magnetostriction enhancement is offset by the coexisting harmful $L1_2$ equilibrium phase (Fig. 6)

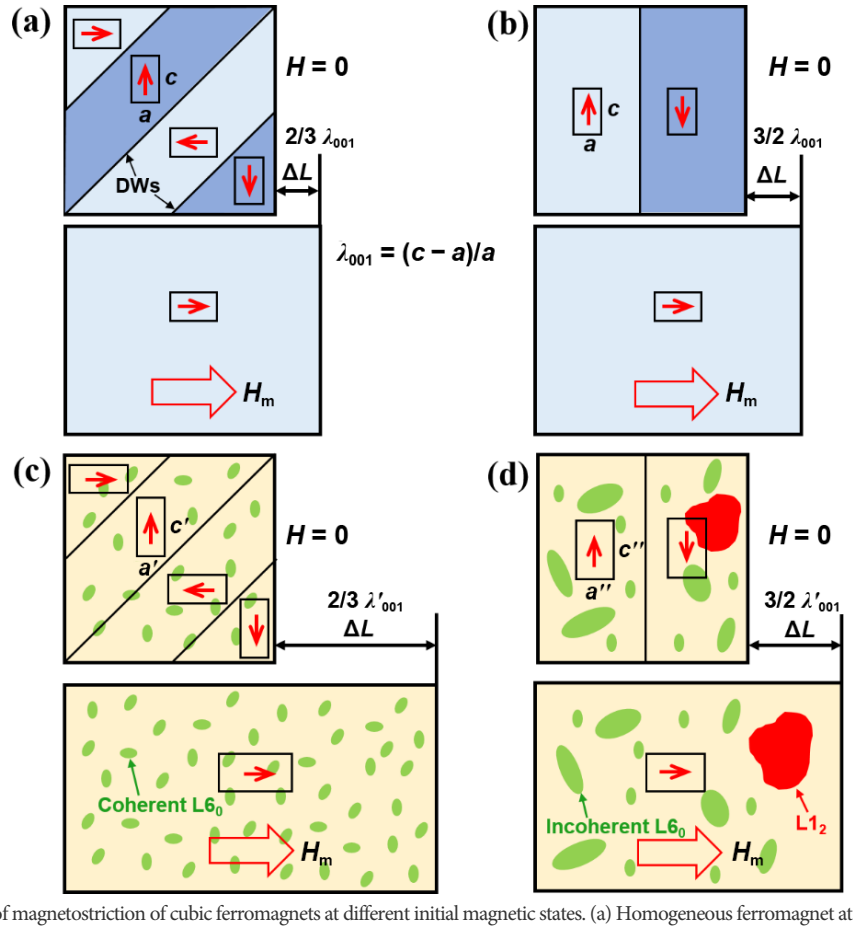

Fig. 7 Schematic diagrams of magnetostriction of cubic ferromagnets at different initial magnetic states. (a) Homogeneous ferromagnet at thermally demagnetized state (upper) and corresponding saturation magnetic state (bottom). (b) Homogeneous ferromagnet with uniaxial magnetic anisotropy (upper) and corresponding saturation magnetic state (bottom). (c) NMHT heterogeneous Fe–Ga alloys with coherent $L6_0$ nanoprecipitates in a thermally demagnetized state (upper) and corresponding saturation magnetic state (bottom). (d) MHT heterogeneous Fe–Ga alloys (incoherent $L6_0/L1_2$ precipitates embedded within matrix with uniaxial magnetic anisotropy) (upper) and corresponding saturation magnetic state (bottom).

since this phase has a negative intrinsic magnetostriction constant, which is opposite to that of the BCC matrix [53]. In addition, it was reported that the $L1_2$ phase has a larger MCA constant K_1 than the BCC matrix [9,54]. Thus, the formation of the $L1_2$ phase and the induced uniaxial magnetic anisotropy contribute to strengthening the effective MCA, thus leading to a larger saturation field in the MHT sample (Fig. 2) than in the NMHT sample.

The comparable microstructure investigations also indicate that, compared with the NMHT process (static heat treatment conditions), applying a strong external magnetic field of 12 T during the heat treatment process induces dynamic precipitation of the $L6_0/L1_2$ phases. Since $L1_2$ is the equilibrium phase (having a lower free energy than the metastable $A2/D0_3$ phases) [55], its precipitation will certainly make the system stable. The free energy difference between the $L1_2$ and $A2/D0_3$ phases then provides the intrinsic driving force. When an external magnetic field is applied during isothermal tempering and slow cooling processes, extra energy alters the free energy profile and solute partitioning below T_C, thus affecting the precipitation thermodynamics and kinetics. The change in precipitation thermodynamics can be attributed to the increased driving force, which includes the intrinsic chemical driving force and the extra magnetostatic energy $-\Delta M{\cdot}H$, where ΔM is the M_s difference between the $L6_0/L1_2$ precipitates and the BCC matrix. At 450 °C (above T_C-$D0_3$), the $L6_0/L1_2$ phases are ferromagnetic, whereas the $D0_3$ phase is paramagnetic (Fig. 1(a)). $\Delta M{\cdot}H$ can be described by M_s-$L6_0/L1_2{\cdot}H$, which acts as the extra driving force. Below T_C-$D0_3$, both the matrix and precipitates are ferromagnetic, and $\Delta M{\cdot}H$ is described by (M_s-$L6_0/L1_2$-M_s-$A2/D0_3$)$\cdot H$. The precipitation of $L6_0$ is associated with local Ga depletion by changing its composition toward stoichiometric Fe_3Ga. This means that an increase in the Fe content of the precipitates favors an increase in their M_s. At the same time, the Ga element expelled from the nanoprecipitates promotes $D0_3$-type ordering of the matrix, which decreases the M_s of the matrix [54]. Therefore, precipitation increases the magnetostatic energy difference between the $L6_0/L1_2$ phases and the matrix. As shown in Fig. 2(b), precipitation of the $L6_0/L1_2$ phases increases the net M_s, and $L6_0/L1_2$ phases should have larger M_s values than $A2/D0_3$ matrix does. Thus, in the ferromagnetic state (cooling below T_C-$D0_3$), the extra magnetostatic energy driving force still works. According to the thermokinetic correlation theory proposed by Huang *et al.* [56,57], an increased thermodynamic driving force accelerates phase transformation kinetics. Consequently, it is not surprising that applying a magnetic field of 12 T (stronger than the saturation magnetic field, see Fig. 2(b)) can induce dynamic precipitation of $L6_0/L1_2$ phases, characterized by coarser $L6_0$ nanoprecipitates than those for the static precipitation case and by the yet-formed $L1_2$ equilibrium phase twins (Fig. 6) that are absent in the NMHT sample. Similar dynamic precipitation behavior has also been reported by other groups. For example, Milyutin *et al.* [58] reported that a large amount of the $L1_2$ phase was formed by aging the $Fe_{73}Ga_{27}$ alloy for 15 min at 450 °C under a strong magnetic field of 25 T, where the $L1_2$ equilibrium phase was found

to appear after aging for a much longer time (12 h) at the same temperature in the absence of a magnetic field. More commonly, the dynamic precipitation induced by thermomagnetic processing is analogous to that induced by thermomechanical processing [59], which has the advantages of shortening the peak aging time and/or lowering the optimum aging temperature. Indeed, in the same composition of $Fe_{73}Ga_{27}$ alloy, either internal stress or external stress provides an extra driving force to induce dynamic precipitation, leading to faster growth kinetics of the $L6_0$ nanoprecipitates than under static aging conditions [14].

To further optimize the magnetostriction performance, the dynamic precipitation processing parameters should be carefully controlled, e.g., by shortening the isothermal aging time, to avoid the overgrowth of coherent nanoprecipitates into incoherent $L6_0$ nanoprecipitates and/or the formation of harmful $L1_2$ equilibrium phase, which awaits future study. In addition, MHT also induces other interesting phenomena, e.g., the formation of only one kind of precipitate variant in local regions. In Fig. 6(b), only type-1 variants are identified in the white circle region (Fig. 6(a)) of the MHT sample, and the other two types observed in the NMHT sample (Fig. 5(b)) are absent. Moreover, the larger precipitates beside the white circle region of Fig. 6(a) are $L1_2$ twin variants. This raises new questions: at what stage are the other types of variants formed, and how do they grow into micron-sized twins? The answers also await further study.

5 Conclusions

A comparative study on the $Fe_{73}Ga_{27}$ alloy showed that performing MHT can simultaneously induce uniaxial magnetic anisotropy and nanoprecipitates, thus increasing the saturation magnetostriction from 65 ppm for the counterpart to 140 ppm by 115%. This demonstrates that combining uniaxial magnetic anisotropy and nanoprecipitates is a feasible way to achieve high-performance magnetostriction in heterogeneous Fe-based alloys. However, care should be taken to control the size, structure, and coherency of the nanoprecipitates carefully since applying a strong magnetic field during the heat-treatment process provides an extra driving force to accelerate the precipitation kinetics (i.e., enable dynamic precipitation), for which the overgrowth of $L6_0$ nanoprecipitates or the formation of the $L1_2$ equilibrium phase may weaken the magnetostriction strengthening effect. The present findings might broaden the knowledge of dynamic precipitation from well-known thermomechanical processing to thermomagnetic processing, especially in magnetic materials.

Acknowledgements

This work was supported by the National Key R&D Program of China (No. 2021YFB3501401) and the National Natural Science Foundation of China (Nos. 52301249 and 52471207).

Author contributions

Ying Chen is responsible for methodology, formal analysis, data curation, and paper writing. Ruihua Qiao is responsible for methodology, investigation, and data curation. Junming Gou is responsible for investigation, formal analysis, and paper writing. Tie Liu is responsible for methodology, investigation, and paper writing. Qiang Wang is responsible for funding acquisition and paper writing. Tianyu Ma is responsible for funding acquisition, conceptualization, and paper writing.

Availability of data and materials

The data that support the findings of this study are available from the corresponding author upon reasonable request.

Competing interests

The authors have no competing interests to declare that are relevant to the content of this article. The author Qiang Wang is the Editorial Committee member of the journal.

References

[1] Nagaska H, Honda K. Magnetostriction of some ferromagnetic substances. *Nature* 1902, **65**: 246.
[2] Meng QK, Dong JT, Nie P, *et al.* Magnetostriction, piezomagnetism and domain nucleation in a Kagome antiferromagnet. *Nat Commun* 2024, **15**: 6921.
[3] Meisenheimer PB, Steinhardt RA, Sung SH, *et al.* Engineering new limits to magnetostriction through metastability in iron-gallium alloys. *Nat Commun* 2021, **12**: 2757.
[4] Patil MA, Kadoli R. Engineers guide to Terfenol-D actuators: Design, performance, and real-world applications. *Sensor Actuator Rep* 2024, **8**: 100236.
[5] Guruswamy S, Srisukhumbowornchai N, Clark AE, *et al.* Strong, ductile, and low-field-magnetostrictive alloys based on Fe–Ga. *Scripta Mater* 2000, **43**: 239–244.
[6] Zhang YQ, Yang TZ, Gou JM, *et al.* Origin of heterogeneous magnetostriction: A case study of nanoprecipitates-bearing Fe–Mo alloys. *J Alloys Compd* 2022, **895**: 162558.
[7] Han YJ, Wang H, Zhang TL, *et al.* Giant magnetostriction in nanoheterogeneous Fe–Al alloys. *Appl Phys Lett* 2018, **112**: 082402.
[8] Cao H, Gehring PM, Devreugd CP, *et al.* Role of nanoscale precipitates on the enhanced magnetostriction of heat-treated Galfenol ($Fe_{1-x}Ga_x$) alloys. *Phys Rev Lett* 2010, **105**: 119904.
[9] Petculescu G, Wu R, McQueeney R. Magnetoelasticity of BCC Fe–Ga alloys. *Handbook of Magnetic Materials* 2012, **20**: 123–226.
[10] Coey JMD. *Magnetism and Magnetic Materials*. Cambridge (UK): Cambridge University Press, 2010
[11] He YK, Ke XQ, Jiang CB, *et al.* Interaction of trace rare-earth dopants and nanoheterogeneities induces giant magnetostriction in Fe–Ga alloys. *Adv Funct Mater* 2018, **28**: 1800858.
[12] Gou JM, Ma TY, Liu XL, *et al.* Large and sensitive magnetostriction in ferromagnetic composites with nanodispersive precipitates. *NPG Asia Mater* 2021, **13**: 6.
[13] He YK, Jiang CB, Wu W, *et al.* Giant heterogeneous magnetostriction in Fe–Ga alloys: Effect of trace element doping. *Acta Mater* 2016, **109**: 177–186.
[14] Gou JM, Ma TY, Qiao RH, *et al.* Dynamic precipitation and the resultant magnetostriction enhancement in [001]-oriented Fe–Ga alloys. *Acta Mater* 2021, **206**: 116631.
[15] Fitchorov TI, Bennett S, Jiang LP, *et al.* Thermally driven large magnetoresistance and magnetostriction in multifunctional magnetic FeGa–Tb alloys. *Acta Mater* 2014, **73**: 19–26.
[16] Chen YJ, Wang JM, Jiang CB. Tailoring ferroic domains by introducing internal stress: $Fe_{81}Ga_{19}$ magnetostrictive alloy as an example. *Appl Phys Lett* 2018, **113**: 112405.
[17] Wu GH, Zhao XG, Wang JH, *et al.* <111> oriented and twin-free single crystals of Terfenol-D grown by Czochralski method with cold crucible. *Appl Phys Lett* 1995, **67**: 2005–2007.
[18] Liu YY, Li JH, Li XL, *et al.* Single Goss grain growth by isothermal annealing in rolled Fe–Al–Ga–NbC sheets. *Rare Metals* 2023, **42**: 3537–3544.
[19] Li ZB, Zhang YD, Esling C, *et al.* Determination of the orientation relationship between austenite and 5M modulated martensite in Ni–Mn–Ga alloys. *J Appl Crystallogr* 2011, **44**: 1222–1226.
[20] Zhang TT, Gong YY, Wang B, *et al.* Crystallography of the martensitic transformation between Ni_2In-type hexagonal and TiNiSi-type orthorhombic phases. *J Mater Sci Technol* 2022, **104**: 59–66.
[21] Zhang CS, Ma TY, Yan M. Induced additional anisotropy influences on magnetostriction of giant magnetostrictive materials. *J Appl Phys* 2012, **112**: 103908.
[22] Ma TY, Yan M, Zhang JJ, *et al.* Differential magnetostrictive response in magnetically annealed $Tb_{0.36}Dy_{0.64}(Fe_{0.85}Co_{0.15})_2$ with <110> crystal orientation. *Appl Phys Lett* 2007, **90**: 102502.

[23] Spaldin NA. Magnetic Materials: Fundamentals and Applications. Cambridge (UK): Cambridge University Press, 2010
[24] Galloway N, Greenough RD, Jenner AGI, *et al.* Pressure dependencies of magnetostrictive strain and *d* coefficient in Terfenol-D after thermal or magnetic annealing. *J Appl Phys* 1994, **76**: 7163–7165.
[25] Galloway N, Schulze MP, Greenough RD, *et al.* Enhanced differential magnetostrictive response in annealed Terfenol-D. *Appl Phys Lett* 1993, **63**: 842–844.
[26] Zhang YQ, Gou JM, Yang TZ, *et al.* Non-equilibrium time-temperature-transformation diagram for enhancing magnetostriction of Fe–Ga alloys. *Acta Mater* 2023, **244**: 118548.
[27] Atulasimha J, Flatau AB. A review of magnetostrictive iron–gallium alloys. *Smart Mater Struct* 2011, **20**: 043001.
[28] Xing Q, Du Y, McQueeney RJ, *et al.* Structural investigations of Fe–Ga alloys: Phase relations and magnetostrictive behavior. *Acta Mater* 2008, **56**: 4536–4546.
[29] Ma TY, Gou JM, Hu SS, *et al.* Highly thermal-stable ferromagnetism by a natural composite. *Nat Commun* 2017, **8**: 13937.
[30] Dong SL, Liu T, Dong M, *et al.* Enhanced magnetostriction of Tb–Dy–Fe via simultaneous <111>-crystallographic orientation and morphological alignment induced by directional solidification in high magnetic fields. *Appl Phys Lett* 2020, **116**: 053903.
[31] Shen P, Zhou D, Liu S, *et al.* Rotation behavior of individual magnetic moment with uniaxial magnetocrystalline anisotropy in magnetic field. *Physica B* 2022, **625**: 413500.
[32] Riego P, Fallarino L, Martínez-Oliver C, *et al.* Magnetic anisotropy of uniaxial ferromagnets near the Curie temperature. *Phys Rev B* 2020, **102**: 174436.
[33] Mukai T, Fujimoto T. Heat-treatment induced anisotropy in Nd–Fe–B magnets prepared from melt-spun ribbons. *J Magn Magn Mater* 1991, **95**: 145–153.
[34] Wang Q, Liu Y, Liu T, *et al.* Magnetostriction of $TbFe_2$-based alloy treated in a semi-solid state with a high magnetic field. *Appl Phys Lett* 2012, **101**: 132406.
[35] Balagurov AM, Samoylova NY, Golovin IS. Diffusive and displacive phase transitions in Fe–Ga alloys. *Physica B* 2024, **676**: 415668.
[36] Ke YB, Wu HH, Lan S, *et al.* Tuning magnetostriction of Fe–Ga alloys via stress engineering. *J Alloys Compd* 2020, **822**: 153687.
[37] Palacheva VV, Emdadi A, Emeis F, *et al.* Phase transitions as a tool for tailoring magnetostriction in intrinsic Fe–Ga composites. *Acta Mater* 2017, **130**: 229–239.
[38] Khachaturyan AG, Viehland D. Structurally heterogeneous model of extrinsic magnetostriction for Fe–Ga and similar magnetic alloys: Part I. Decomposition and confined displacive transformation. *Metall Mater Trans A* 2007, **38**: 2308–2316.
[39] Kawamiya N, Adachi K, Nakamura Y. Magnetic properties and mössabauer investigations of Fe–Ga alloys. *J Phys Soc Jpn* 1972, **33**: 1318–1327.
[40] Srisukhumbowornchai N, Guruswamy S. Influence of ordering on the magnetostriction of Fe–27.5 at% Ga alloys. *J Appl Phys* 2002, **92**: 5371–5379.
[41] Jayaraman TV, Corson RP, Guruswamy S. Ordering, magnetostriction, and elastic properties in Fe–27.5 at% Ga alloy single crystals. *J Appl Phys* 2007, **102**: 053905.
[42] Gou JM, Yang TZ, Qiao RH, *et al.* Formation mechanism of tetragonal nanoprecipitates in Fe–Ga alloys that dominate the material's large magnetostriction. *Scripta Mater* 2020, **185**: 129–133.
[43] Gou JM, Yang TZ, Liu XL, *et al.* Internal structure evolution of $L1_2$ variants in aged Fe–Ga alloys. *J Alloys Compd* 2020, **836**: 155282.
[44] Wu RQ. Origin of large magnetostriction in FeGa alloys. *J Appl Phys* 2002, **91**: 7358–7360.
[45] Yang S, Ren XB. Noncubic crystallographic symmetry of a cubic ferromagnet: Simultaneous structural change at the ferromagnetic transition. *Phys Rev B* 2008, **77**: 014407.
[46] Qiao BY, Zhao SY, Yao JC, *et al.* Highly stable magnetostriction in nanoheterogeneous $Fe_{81}Ga_{19}$ alloy enabled by uncoarsening of nanoprecipitates due to negative interfacial energy. *Adv Funct Mater* 2024: 2419157.
[47] He YK, Coey JMD, Schaefer R, *et al.* Determination of bulk domain structure and magnetization processes in BCC ferromagnetic alloys: Analysis of magnetostriction in $Fe_{83}Ga_{17}$. *Phys Rev Mater* 2018, **2**: 014412.
[48] Wu YY, Chen YJ, Meng CZ, *et al.* Multiscale influence of trace Tb addition on the magnetostriction and ductility of <100> oriented directionally solidified Fe–Ga crystals. *Phys Rev Materials* 2019, **3**: 033401.
[49] Ren XB. Large electric-field-induced strain in ferroelectric crystals by point-defect-mediated reversible domain switching. *Nat Mater* 2004, **3**: 91–94.
[50] Aaronson HI, Enomoto M, Lee JK. *Mechanisms of Diffusional Phase Transformations in Metals and Alloys*. New York (USA): CRC Press, 2010.
[51] Chen YJ, Fu ZH, Wu YY, *et al.* Giant heterogeneous magnetostriction induced by charge accumulation-mediated nanoinclusion formation in dual-phase nanostructured systems. *Acta Mater* 2021, **213**: 116975.
[52] Zhang CS, Gou JM, Yang JJ, *et al.* Nanoheterogeneity response in large-magnetostriction Fe–Ga alloys: An *in situ* magnetic small-angle neutron scattering study. *Acta Mater* 2022, **225**: 117594.
[53] Vershinina TN, Samoylova NY, Sumnikov SV, *et al.* Comparative study of structures and phase transitions in Fe–(31–35) at% Ga alloys by *in situ* neutron diffraction. *J Alloys Compd* 2023, **934**: 167967.
[54] Gou JM, Liu XL, Wu KY, *et al.* Tailoring magnetostriction sign of ferromagnetic composite by increasing magnetic field strength. *Appl Phys Lett* 2016, **109**: 082404.
[55] Lograsso TA, Ross AR, Schlagel DL, *et al.* Structural transformations in quenched Fe–Ga alloys. *J Alloys Compd* 2003, **350**: 95–101.
[56] Huang LK, Liu X, Niu K, *et al.* Thermo-kinetic insights into deformation mechanism in the phase-transforming nanostructured Fe alloy. *Acta Mater* 2024, **279**: 120311.
[57] Huang LK, Guo C, Liu YT, *et al.* Grain refinement tailoring the kinetics of phase transformation in nanograined Fe alloy: Smaller is slower. *Scripta Mater* 2022, **221**: 114948.
[58] Milyutin VA, Gervasyeva IV, Shishkin DA, *et al.* Effect of high magnetic field on the phase transition in Fe–24%Ga and Fe–27%Ga during isothermal annealing. *J Magn Magn Mater* 2020, **514**: 167284.
[59] Muhammad A, Sato-Turtelli R, Kriegisch M, *et al.* Large enhancement of magnetostriction due to compaction hydrostatic pressure and magnetic annealing in $CoFe_2O_4$. *J Appl Phys* 2012, **111**: 013918.

Ying Chen received her master degree from Northwestern Polytechnical University, China, in 2023. Since 2023, she has been a Ph.D. candidate at Xi'an Jiaotong University, China. Her research interests include magnetostrictive materials, functional high-entropy alloys, and solid-state phase transitions. She has published six papers in academic journals, including *Advanced Materials, Wear, Journal of Alloys Compounds*, and *Surface & Coatings Technology*.

Tianyu Ma received his Ph.D. degree from Beihang University (formerly Beijing University of Aeronautics and Astronautics), China, in 2006. From 2011 to 2013, he worked at the National Institute for Materials Science, Japan, as a Japan society for the promotion of science (JSPS) foreign postdoc. Since 2017, he has been a professor at Xi'an Jiaotong University, China. His research interests include magnetostrictive materials, shape memory alloys, rare-earth hard magnets, functional high-entropy alloys, and solid-state phase transitions. He has published over 200 papers in academic journals, including *Nature*, *Nature Communications*, *Advanced Materials*, and *Acta Materialia*.